Modelling dynamic cable-sheave contact and detachment during towing operations

Cassidy Westin*, Rishad A. Irani

Department of Mechanical and Aerospace Engineering, Carleton University, 1125 Colonel By Drive, Ottawa, Canada, K1S 5B6

Abstract

Cable-sheave systems are commonly used on marine vessels for lifting and towing applications. As a result of the motion of the vessel, the cable can detach from the surface of the sheave. This paper presents a finite element model of a towed cable system based on the Absolute Nodal Coordinate Formulation. The model includes the interaction of the cable with the sheave surface in order to examine variations in the contact forces. Furthermore, a three-dimensional description of the sheave geometry is implemented in order to accurately model the contact forces as the vessel undergoes six degree-of-freedom motion. To assess the performance of the model, the simulated cable behavior is compared to small scale experimental measurements. Finally, a case study which demonstrates the simulated cable detachment behavior for a full scale system is discussed.

Key words: Towed cables, modelling, dynamic contact, non-linear finite elements, cable-sheave interaction, detachment

1. Introduction

Cable-pulley systems are commonly used in marine lifting applications and towing of sensor bodies for oceanographic research. Figure 1 illustrates a vessel towing a submerged sensor with a cable. A sheave is used to position the cable

*Corresponding author.
Email addresses: cassidy.westin@carleton.ca (Cassidy Westin), rishad.irani@carleton.ca (Rishad A. Irani)

over the stern of the vessel, while a winch is used to pay-out and reel-in the cable. The cable experiences hydrodynamic drag, forming a catenary as shown in the figure, as well as forces transmitted through the sheave due to the motion of the ship. As a result of the ship motion, the cable can experience large variations in tension and is susceptible to loss of contact with the sheave surface if the tension becomes small. For many systems it may not be possible to constrain the cable in the sheave mechanically. It is thus desirable to model the cable dynamics and interactions with the sheave and winch surfaces in order to predict cable detachment and avoid unsafe conditions.

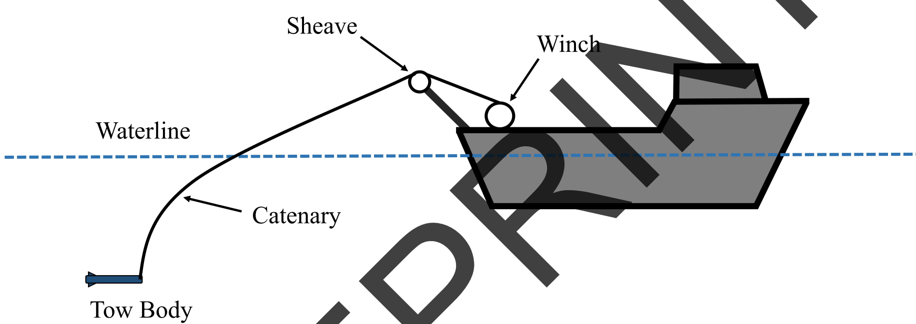

Figure 1: Diagram of ship and towed cable

Various modelling methods including both Finite Difference Methods (FDM) and Finite Element Methods (FEM) have been used to simulate the dynamics of marine cables, however nonlinear finite element models are prevalent for modeling cable-pulley systems. The continuous nature of curved element formulations is advantageous, as the contact forces can be defined as continuous functions of the cable position, velocity. Thus, only a small number of elements are required to accurately model the cable-pulley interaction compared to linear methods. In the recent literature, the Absolute Nodal Coordinate Formulation (ANCF) is common for modeling both submerged cables [1, 2] and cable-pulley interactions [3–5].

Finite element models of submerged cables typically use a revolute joint to model the attachment of the cable to the ship. A model of a submerged cable that includes the interaction of the cable with the winch and sheave has not been found in the literature. However, a number of systems consisting of a cable with surface contact have been examined including belt-drives [6, 7], catenary-pantograph interactions [8] and loaded cable-pulley systems [3–5]. These studies usually only consider static loads or simple, planar cable motions. Also, the cable motion in these systems is often purely reciprocal and the area of contact between the cable and the surface remains constant. A small number of studies have examined cable-pulley interactions with dynamic contact [5, 9].

A model of a towed cable system which includes both the dynamics of the submerged cable, the towbody and the normal contact between the cable and the sheave could be used to examine dynamic contact behavior and cable detachment during towing operations. This paper presents a mathematical model and simulation of a towed cable which utilizes the nonlinear ANCF finite element method. Moreover, this paper outlines how the ANCF model was parameterized, tuned and implemented. The research builds upon previous marine cable models by introducing the interaction between the cable and the sheave and winch surfaces using a penalty contact formulation. Additionally, in contrast to the planar cable-pulley models found in the literature, a three dimensional formulation of the contact forces between the cable and the sheave groove is developed. The three dimensional formulation enables accurate modelling of the contact forces during six degree-of-freedom ship motion. Finally, the ability of the contact formulation to simulate dynamic contact behavior and detachment of the cable from the sheave during towing operations is examined.

Section 2 of this paper details the formulation of the cable model and its computer implementation. In Section 3, the results of a small scale experiment are compared to the simulated cable behavior. A full scale case study which demonstrates the cable detachment behavior is described in Section 4. The paper ends with concluding remarks and recommendations for future work in Section 5.

2. Modelling

The finite element model follows the Absolute Nodal Coordinate Formulation [10] and is composed of two node cable elements. Each node has 6 degrees of freedom consisting of a 3×1 position vector $\mathbf{r}$ and a 3×1 slope vector $\mathbf{r}'$ tangent to the cable centerline. All degrees of freedom are defined in the absolute (or inertial) coordinate frame. Figure 2 shows a deformed cable element with arc length s at the top and the equivalent undeformed element with unstretched length L at the bottom. The nodes located at either end of the element are represented by closed circles.

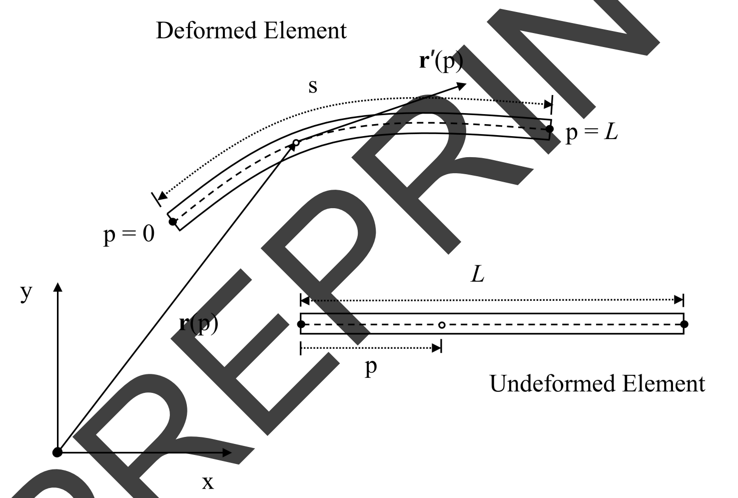

Figure 2: Deformed cable element and equivalent undeformed element in the inertial coordinate frame.

The absolute coordinates $\mathbf{r}$ of an arbitrary point on the cable can be interpolated from the set of nodal degrees of freedom using the arc parameter $p \in [0, L]$:

$$\mathbf{r}(p) = \mathbf{S}(p)\mathbf{q} = [x \quad y \quad z]^T. \tag{1}$$

where $\mathbf{S}(p)$ is a shape function matrix and $\mathbf{q}$ is a column vector of generalized coordinates collecting the 12 element degrees of freedom. The generalized coordinates consist of the Cartesian coordinates $\mathbf{r}$ and the parametric slopes $\mathbf{r}_p = \partial \mathbf{r}/\partial p$ at each node,

$$\mathbf{q} = \left[\mathbf{r}(0)^T \quad \mathbf{r}_p(0)^T \quad \mathbf{r}(L)^T \quad \mathbf{r}_p(L)^T\right]^T. \tag{2}$$

The shape function matrix $\mathbf{S}(p)$ representing a cubic Hermite spline is

$$\mathbf{S}(p) = \begin{bmatrix} \left(1 - 3\xi^2 + 2\xi^3\right)\mathbf{I} \\ \left(\xi - 2\xi^2 + \xi^3\right)\mathbf{I} \\ \left(3\xi^2 - 2\xi^3\right)\mathbf{I} \\ \left(-\xi^2 + \xi^3\right)\mathbf{I} \end{bmatrix}^T \tag{3}$$

where $\mathbf{I}$ is a 3x3 identity matrix and $\xi = p/L$ is the parameter p normalized by the unstretched element length.

The generalized Newton-Euler equations are given for a single element as

$$\mathbf{M}\ddot{\mathbf{q}} + \mathbf{Q}_{\text{int}} - \mathbf{Q}_{\text{ext}} = 0, \tag{4}$$

where $\mathbf{M}$ is the mass matrix, $\mathbf{Q}_{\text{int}}$ is a generalized internal force vector, $\mathbf{Q}_{\text{ext}}$ is a generalized external force vector. The internal forces consist of the elastic forces $\mathbf{Q}_e$ and a damping force $\mathbf{Q}_d$. The external forces consist of hydrodynamic, contact and gravitational forces.

Given a distributed force per unit length $\mathbf{f}(p)$, the generalized force vector $\mathbf{Q}$ can be determined by premultiplying by the transpose of the shape function and integrating over the length of the element [11]:

$$\mathbf{Q}_i = \int_0^L \mathbf{S}^T \mathbf{f}_i(p)dp. \tag{5}$$

In this work, the integral is approximated using a numerical quadrature

$$\mathbf{Q}_i \approx \frac{L}{N_I}\sum_0^{N_I} w_i \mathbf{S}^T \mathbf{f}(p_i), \tag{6}$$

where N_I is the number of integration points, p_i is the value of the arc parameter at point i and w_i represent the trapezoidal weights given by

$$w_i = \begin{cases} 0.5, & i = 1, N_I \\ 1, & i = 2, ..., N_I - 1 \end{cases}. \tag{7}$$

The following section outlines the various force components found in Equation 4.

2.1. Mass Matrix and Internal Forces

Using a variational mass lumping approach the mass matrix $\mathbf{M}$ is derived directly from the element kinetic energy [10] and is given by

$$\mathbf{M} = \frac{\partial^2 K}{\partial \dot{\mathbf{q}} \partial \dot{\mathbf{q}}} = \int_0^L \rho A \mathbf{S}(\mathbf{p})^T \mathbf{S}(\mathbf{p}) dp \tag{8}$$

where K is the kinetic energy of the element, ρ is the cable density and A is the cable cross-sectional area.

Similarly, the elastic forces $\mathbf{Q}_e$ are derived from the strain energy U of the element and are given by [12]:

$$\mathbf{Q}_e = \frac{\partial U}{\partial \mathbf{q}} = \int_0^L \left[EA\varepsilon \frac{\partial \varepsilon}{\partial \mathbf{q}} + EI\kappa \frac{\partial \kappa}{\partial \mathbf{q}} \right] dp \tag{9}$$

where E is the Young's modulus of the cable material, A is the cross-sectional area, I is the second moment of area, ε is the longitudinal strain, and κ is the curvature of the element.

Berzeri and Shabana [12] define ε as the Green-Lagrange strain given by

$$\varepsilon = \frac{1}{2}(\mathbf{r}_p{}^T \mathbf{r}_p - 1). \tag{10}$$

However, using the above strain definition results in coupling of the longitudinal strains to the element curvature, since the slope vector $\mathbf{r}_p$ defines not only the shape of the element, but the distribution of strain across the element. As a result, an element with no overall strain (i.e. an arc length equal to the unstretched length L) but a non-zero curvature will have non-zero strain along its length. The coupling of the longitudinal and bending deformations leads to increased stiffness of the numerical solution in addition to erroneous cable tensions in elements with significant curvatures.

It is desirable to decouple the longitudinal strains from the curvature. Yue et al. [13] present an alternative stiffness force definition that alleviates the coupled behavior. First a secondary set of generalized coordinates $\mathbf{q}^{\Delta}$, representing only the longitudinal deformation of the ANCF cable element, is defined as

$$\mathbf{q}^{\Delta} = \begin{bmatrix} 0 & |\mathbf{r}'(0)| & \int_0^L |\mathbf{r}'(p)|dp & |\mathbf{r}'(L)| \end{bmatrix}^T . \tag{11}$$

This formulation of the coordinates represents a one-dimensional cable element that is parameterized equivalent to the full ANCF element. Thus, the longitudinal coordinate of an arbitrary point on the element is given by

$$r^{\Delta} = \mathbf{S}^{\Delta}\mathbf{q}^{\Delta} \tag{12}$$

where $\mathbf{S}^{\Delta}$ is the one-dimensional shape function

$$\mathbf{S}^{\Delta} = \begin{bmatrix} (1 - 3\xi^2 + 2\xi^3) & (\xi - 2\xi^2 + \xi^3) & (3\xi^2 - 2\xi^3) & (-\xi^2 + \xi^3) \end{bmatrix} . \tag{13}$$

The one-dimensional coordinate r^{Δ} is then substituted into the Green-Lagrange strain (Equation 10) giving a decoupled longitudinal strain ε^{Δ}

$$\varepsilon^{\Delta} = \frac{1}{2}\left[\left(\frac{\partial r^{\Delta}}{\partial p}\right)^2 - 1\right] = \frac{1}{2}\left[(\mathbf{S}_p^{\Delta}\mathbf{q}^{\Delta})^T(\mathbf{S}_p^{\Delta}\mathbf{q}^{\Delta}) - 1\right] \tag{14}$$

where the subscript p represents the derivative with respect to p. The decoupled strain ε^{Δ} is then substituted for ε in Equation 9.

Berzeri and Shabana [12] utilize the Seret-Frenet definition of the element curvature κ given by

$$\kappa = \left|\frac{d\mathbf{r}^2}{ds^2}\right| = \frac{|\mathbf{r}_p \times \mathbf{r}_{pp}|}{|\mathbf{r}_p|^3} \tag{15}$$

where s is the arc length and $\mathbf{r}_p$ and $\mathbf{r}_{pp}$ are the first and second partial derivatives of $\mathbf{r}$ with respect to p [12]. Berzeri and Shabana [12] also propose a simplification of Equation 9 by assuming that the longitudinal deformations are small (i.e. $|\mathbf{r}_p| \approx 1$), in which case the curvature simplifies to

$$\kappa \approx |\mathbf{r}_{pp}|. \tag{16}$$

The simplified curvature is used in the current study to reduce the computational cost of the simulation.

The internal damping force $\mathbf{Q}_d$ serves to include internal energy dissipation as well as improve the numerical stability of the simulation. For submerged cables it is common to neglect the internal cable damping [14] since the external fluid damping dominates. However, in the current work the inclusion of internal damping was found to have a significant effect on the numerical stiffness and stability of the simulation. Additionally, the damping effects may be significant in the unsubmerged section of the cable; thus, internal damping was implemented based on a Rayleigh dissipation function.

The Rayleigh dissipation function represents one-half of the energy dissipated during the motion and has a general form

$$R = 1/2 \int c\dot{u}^2 dV \tag{17}$$

where c is a damping factor and $\dot{u}$ is the rate of change of a chosen coordinate u [15]. In the current study, the generalized coordinate u is chosen to be the gradient $\mathbf{r}_p = \partial\mathbf{r}/\partial p$, where $\mathbf{r}$ is the absolute position of a cable segment, such that energy is dissipated if during bending and axial deformations. The energy dissipation will also occur during rigid body rotations, however the additional dissipation can be viewed as viscous damping due to air or water resistance. Substituting $u = \mathbf{r}_p$ into Equation 17, the Rayleigh dissipation function becomes

$$R = 1/2 \int_0^L c(\dot{\mathbf{r}}_p \cdot \dot{\mathbf{r}}_p) dp. \tag{18}$$

The damping force $\mathbf{Q}_d$ is then given by

$$\mathbf{Q}_d = \frac{\partial R}{\partial \dot{\mathbf{q}}} = c \int_0^L \mathbf{S}_p^T \mathbf{S}_p dp \, \dot{\mathbf{q}}. \tag{19}$$

The estimation of the damping coefficient c based on the cable damping ratio is further discussed in Section 3.2. In the next section, the external hydrodynamic forces are defined.

2.2. Hydrodynamic Forces

For the portion of the cable that is submerged in water, the external hydrodynamic force per unit length $\mathbf{f}_H$ consists of three components: the drag force $\mathbf{f}_D$, the inertia force $\mathbf{f}_I$ and the buoyancy force $\mathbf{f}_B$, such that

$$\mathbf{f}_H = \mathbf{f}_D + \mathbf{f}_I + \mathbf{f}_B. \tag{20}$$

For the cable segment above the waterline, $\mathbf{f}_H$ is set to zero.

The buoyancy force is given by Archimedes' principal,

$$\mathbf{f}_B = -\rho_f A \mathbf{g} \tag{21}$$

where $\mathbf{g} = [0 \quad 0 \quad -9.81]^T$ m/s^2 is the gravitational acceleration vector, ρ_f is the fluid density and A is the cable corss-sectional area.

The drag forces used in the current work are based on the model employed by Driscoll and Nahon [16] and Buckham et al. [17]. The model accounts for the nonlinear decomposition of the drag force into normal and tangential components and exhibits good agreement with experimental studies of drag forces on towed cables over a wide range of towing conditions [16]. The components of the drag force are

$$\mathbf{f}_{D,n} = -\frac{1}{2}\rho_f d C_D |\mathbf{V}|^2 \frac{\mathbf{V}_n}{|\mathbf{V}_n|} f_n \tag{22a}$$

$$\mathbf{f}_{D,t} = -\frac{1}{2}\rho_f d C_D |\mathbf{V}|^2 \frac{\mathbf{V}_t}{|\mathbf{V}_t|} f_t \,\mathrm{sgn}(\mathbf{V}_t \cdot \mathbf{u}_t) \tag{22b}$$

where d is the cable diameter, C_D is a drag coefficient, $\mathbf{V} = \mathbf{V}_f - \dot{\mathbf{r}}$ is the difference between the flow velocity $\mathbf{V}_f$ and the cable velocity $\dot{\mathbf{r}}$, f_n and f_t are normal and tangential empirical loading functions, $\mathbf{V}_n$ and $\mathbf{V}_t$ are the normal and tangential components of $\mathbf{V}$ given by

$$\mathbf{V}_t = (\mathbf{V} \cdot \mathbf{u}_t)\mathbf{u}_t \tag{23a}$$

$$\mathbf{V}_n = \mathbf{V} - \mathbf{V}_t \tag{23b}$$

and $\mathbf{u}_t = \mathbf{r}_p / |\mathbf{r}_p|$ is the unit tangent vector along the cable centerline [17]. Figure 3 illustrates the absolute and relative flow velocity vectors and their components normal and tangential to the cable element. The absolute flow velocity vector $\mathbf{V}_f$ is shown as a solid blue line and the relative flow velocity vectors $\mathbf{V}$ is shown as a solid red line. The normal and tangential components of the fluid velocity $\mathbf{V}_{f,n}$ and $\mathbf{V}_{f,t}$ and of the relative velocity $\mathbf{V}_n$ and $\mathbf{V}_t$ are shown as dotted lines.

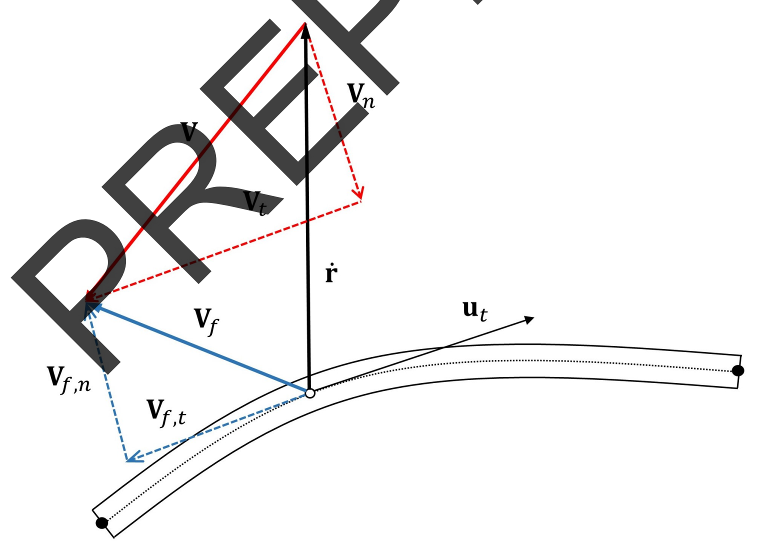

Figure 3: Absolute flow and relative flow velocity vectors in relation to a cable element. The cable velocity $\dot{\mathbf{r}}$, fluid velocity $\mathbf{V}_f$ and relative velocity between the cable and fluid $\mathbf{V}$ are shown as solid lines. The normal and tangential components of the fluid velocity $\mathbf{V}_{f,n}$ and $\mathbf{V}_{f,t}$ and of the relative velocity $\mathbf{V}_n$ and $\mathbf{V}_t$ are shown as dotted lines.

Various experimental studies of submerged cables [18, 19] show that the *mean* drag acting on the cable can be much higher than for rigid cylinders. The increase in drag is a result of vibration of the cable due to vortex shedding. An additional force $\mathbf{f}_{D,amp}$ is applied to the cable to capture the drag amplification due to vortex-induced vibrations (VIV). The additional force is defined as

$$\mathbf{f}_{D,amp} = G(\overline{\mathbf{f}}_{D,n} + \overline{\mathbf{f}}_{D,t}) \tag{24}$$

where G is an amplification factor and $\overline{\mathbf{f}}_{D,n}$ and $\overline{\mathbf{f}}_{D,t}$ are the steady state values of normal and tangential drag forces, which are obtained using Equation 22 with the cable velocity $\dot{\mathbf{r}}$ set to zero. In this implementation, only the mean component of the drag force is amplified and not the transient components.

The total drag force per unit length $\mathbf{f}_D$ from Equation 20 is

$$\mathbf{f}_D = \mathbf{f}_{D,n} + \mathbf{f}_{D,t} + \mathbf{f}_{D,amp}. \tag{25}$$

Within Equation 20, the non-drag terms in the Morison equation are collectively referred to as the inertia force $\mathbf{f}_I$ given by

$$\mathbf{f}_I = \rho_f A C_m(\dot{\mathbf{V}}_{f,n} - \ddot{\mathbf{r}}_n) + \rho_f A \dot{\mathbf{V}}_{f,n} \tag{26}$$

where C_m is the hydrodynamic mass coefficient, $\dot{\mathbf{V}}_{f,n}$ is the acceleration of the flow normal to the cable, and $\ddot{\mathbf{r}}_n = (1 - \mathbf{u}_t^T \mathbf{u}_t)\mathbf{S}\ddot{\mathbf{q}}$ is the normal component of the cable acceleration [20].

Note that the component of the inertia force $\mathbf{f}_I$ that is proportional to the cable's normal acceleration $\ddot{\mathbf{r}}_n$ can be combined with the d'Alembert force $\mathbf{M}\ddot{\mathbf{q}}$ to form a modified mass matrix $\mathbf{M}'$

$$\mathbf{M}' = \mathbf{M} + \rho_f A C_m \int_0^L (1 - \mathbf{u}_t^T \mathbf{u}_t)\mathbf{S}(p)dp, \tag{27}$$

thereby retaining the explicit form of the equations of motion shown in Equation 4. The hydrodynamic forces acting on the towbody are described in the following section.

2.3. Towbody

The towbody is treated as a lumped mass coincident with the last node of the cable. The total force acting on the towbody is given by the sum of the buoyancy, gravitational, d'Alembert and hydrodynamic forces, which follow from the Morison equation. The net force is

$$\mathbf{F}_b = \mathbf{F}_{b,g} + \mathbf{F}_{b,D} + \mathbf{F}_{b,I} + \mathbf{F}_{b,m}, \tag{28}$$

where $\mathbf{F}_{b,g}$ is the net force due to gravity and buoyancy, $\mathbf{F}_{b,I}$ is the inertia force, $\mathbf{F}_{b,m}$ is the force due to hydrodynamic added mass and the d'Alembert force due to the body's inertia.

The gravitational and buoyancy force $\mathbf{F}_{b,g}$ is given by

$$\mathbf{F}_{b,g} = (-\rho_f V + m_b)\mathbf{g}, \tag{29}$$

where V is the volume of the body and m_b is the mass.

The drag force $\mathbf{F}_{b,D}$ is

$$\mathbf{F}_{b,D} = \frac{1}{2}\rho_f(\mathbf{A}_b \circ \mathbf{C}_{D,b}) \circ |\mathbf{V}_f - \mathbf{V}_b|(\mathbf{V}_f - \mathbf{V}_b), \tag{30}$$

where $\mathbf{V}_f$ is the flow velocity and $\mathbf{V}_b$ is the velocity of the end of the cable where the towbody is located. Since the geometry of the body may vary along each axis, $\mathbf{A}_b$ is a vector of areas found by projecting that volume of the body onto the absolute planes, $\mathbf{C}_{D,b}$ is a vector of drag coefficients for each coordinate axis. The symbol $\circ$ represents the entry-wise product, where for $\mathbf{C} = \mathbf{A} \circ \mathbf{B}$ the i-th element of $\mathbf{C}$ is defined as $C_i = A_i B_i$.

The inertia force $\mathbf{F}_{b,I}$ is given by

$$\mathbf{F}_{b,I} = \rho_f V(\mathbf{C}_{m,b} + 1) \circ \dot{\mathbf{V}}_f, \tag{31}$$

where $\mathbf{C}_{m,b}$ is a vector of inertia coefficients for each coordinate axis.

The force due to the hydrodynamic added mass and the d'Alembert force due to the body's inertia $\mathbf{F}_{b,m}$ given by

$$\mathbf{F}_{b,m} = -(m_b \mathbf{I}_{3\times 1} + \rho_f V \mathbf{C}_{m,b}) \circ \dot{\mathbf{V}}_b. \tag{32}$$

Thus, the equivalent generalized force $\mathbf{Q}_b$ acting on the final cable element is

$$\mathbf{Q}_b = \mathbf{S}(L)^T \mathbf{F}_b = \mathbf{S}(L)^T (\mathbf{F}_{b,g} + \mathbf{F}_{b,D} + \mathbf{F}_{b,I} + \mathbf{F}_{b,m}). \tag{33}$$

Additionally, the modified mass matrix $\mathbf{M}'$ from Equation 27 can be further modified to include the towbody inertia force $\mathbf{F}_{b,m}$ as follows:

$$\mathbf{M}'' = \mathbf{M}' + \mathbf{S}(L)^T \mathrm{diag}(m_b \mathbf{I}_{3\times 1} + \rho_f V \mathbf{C}_{m,b}) \mathbf{S}(L). \tag{34}$$

In the following section, the cable-surface interactions and normal contact forces are described.

2.4. Normal Contact

In order to model the cable-sheave and cable-winch interactions, a contact penalty is used. The cable is allowed to "penetrate" the sheave surface and the normal force is defined as a function of the relative penetration δ. The normal force per unit length $\mathbf{f}_N$ acting at a single point on the element is defined using a contact force model developed by Hunt and Crossley [21], which has been used by Bulín et al. [5] and Lugris et al. [3] to model cable-pulley interactions in ANCF cable simulations. The Hunt-Crossley contact model [21] represents the surface as a nonlinear spring-damper with the force per unit length acting on the cable given by

$$\mathbf{f}_N = k_N \delta^n (1 + D\dot{\delta}) \mathbf{u}_N \tag{35}$$

where $\mathbf{u}_N$ is the unit vector normal to the sheave surface at the point of contact, k_N is the contact stiffness, δ is the relative "penetration" of the node into the surface, D is a contact damping coefficient and n is a positive constant. The value of n is typically based on empirical investigations of the evolution of the contact force between two bodies during an impact and may be a function of body geometry and material properties [22]. In the present analysis, a value of $n = 1.5$ is used based the value used by Bulín et al. [5] to model cable-sheave contact.

The relative position vector between an arbitrary "contact point" on the cable and the center of the sheave or winch $\mathbf{s}_{rel}$ is

$$\mathbf{s}_{rel} = \mathbf{s} - \mathbf{s}_c \tag{36}$$

where $\mathbf{s}$ is the position of the cable segment in the ship's body-fixed frame and $\mathbf{s}_c$ is the position of the centroid of the winch or sheave. The contact forces are calculated first by transforming the relative position $\mathbf{s}_{rel}$ from the XYZ coordinate frame onto a fixed plane by rotating about the axis of rotation of the winch or sheave. The fixed plane for the current work is selected to be the YZ plane. Figure 4 shows the transformation of the contact point from XYZ space onto the YZ plane by rotating the relative position $\mathbf{s}_{rel}$ about the winch/sheave axis of rotation, as viewed along the Y-axis. The angle between $\mathbf{s}_{rel}$ is denoted θ_{YZ} and the rotated vector $\mathbf{p}$ is shown as a red arrow. The planar contact forces are then calculated based on the two-dimensional cross-section of the surface in the selected plane. Lastly, the contact force is then transformed to the absolute frame.

The rotation angle θ_{YZ} is

$$\theta_{YZ} = \mathrm{sgn}(X_{rel}) \cos^{-1}\left(\frac{Z_{rel}}{X_{rel}^2 + Z_{rel}^2}\right) \tag{37}$$

where X_{rel} and Z_{rel} are the components of $\mathbf{s}_{rel}$ in the X and Z axes. The rotated vector $\mathbf{p}$ is

$$\mathbf{p} = \mathbf{R}_y(\theta_{YZ})\mathbf{s}_{rel} \tag{38}$$

where $\mathbf{R}_y$ is the rotation matrix about the Y axis. The penetration δ of the

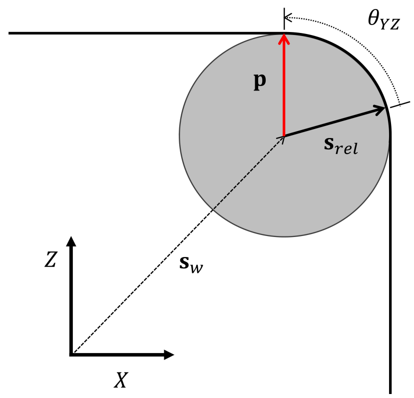

Figure 4: Transformation of contact point from XYZ space to the YZ plane as viewed along the Y-axis. Note that the Y component is unchanged by the transformation.

cable into the surface is

$$\delta = -(\mathbf{p} - \mathbf{p}_0) \cdot \mathbf{n} \tag{39}$$

where $\mathbf{n}$ is a unit vector normal to the contact surface in the YZ-plane and $\mathbf{p}_0$ is a nominal vector given by

$$\mathbf{p}_0 = [0 \quad 0 \quad r + d/2]^T \tag{40}$$

and r is the radius of the winch or sheave. In the latter case, r is measured to the root of the sheave groove.

Figure 5 illustrates the sheave (top) and winch (bottom) contact surfaces. The winch is idealized as an infinite cylinder. Note that since the contact forces are applied at the cable centerline, the “contact surface”, shown as a dotted line, is offset from the actual surface by the radius of the cable. The unit vector normal to the winch contact surface in the YZ-plane is

$$\mathbf{n}^w = [0 \quad 0 \quad 1]^T. \tag{41}$$

In order to accurately model the interaction between the cable and the

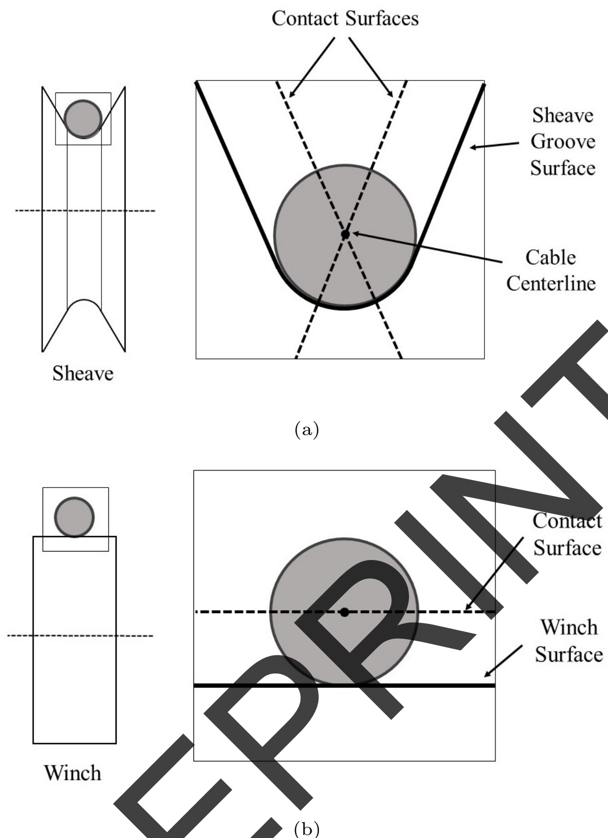

Figure 5: Sheave (a) and winch (b) surface cross-sections. Real surfaces are shown as solid lines. Offset contact surfaces are shown as dotted lines.

sheave, the angled and curved surface of the sheave groove is represented by two straight lines parallel to the straight walls of the groove. Figure 5 shows the contact surfaces as dotted lines and the actual surface of the groove as a solid line. Figure 6 shows the penetration of the cable centerline below the contact surfaces. The contact surfaces, labeled $s1$ and $s2$, intersect at the point $\mathbf{p}_0$ and have normal vectors $\mathbf{n}^{s1}$ and $\mathbf{n}^{s2}$:

$$\mathbf{n}^{s1} = [0 \quad \cos(\theta_g/2) \quad \sin(\theta_g/2)]^T \tag{42a}$$

$$\mathbf{n}^{s2} = [0 \quad -\cos(\theta_g/2) \quad \sin(\theta_g/2)]^T \tag{42b}$$

where θ_g is the throat angle of the groove. The groove surface is idealized such that the radius of curvature of the groove is assumed to be equal to the radius of the cable. The two contact surfaces intersect at the center of curvature of the groove.

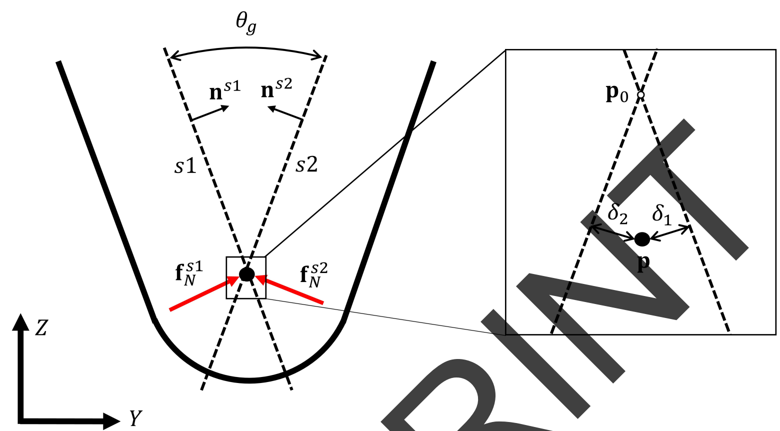

Figure 6: Sheave groove contact.

If the cable centerline lies below either of the dotted lines ($\delta > 0$), a penalty force is produced proportional to the penetration. If the centerline lies above the lines ($\delta < 0$), no normal force is applied. Additionally, if the magnitude of the components of $\mathbf{p}$ exceed specified values, no force is applied, such that the width and height of the sheave groove is limited.

The unit vector $\mathbf{u}_N$ gives the direction of the force in the absolute frame, and is found by rotating the surface normal vector $\mathbf{n}$ by the inverse of the rotation $\mathbf{R}_y(\theta_{YZ})$ applied in Equation 38 and then rotating from the body-fixed frame to the absolute frame with the rotation matrix $\mathbf{R}_B^A(\alpha, \beta, \gamma)$ where α, β and γ are the roll, pitch and yaw of the ship. The unit normal in the absolute frame is thus

$$\mathbf{u}_N = \mathbf{R}_B^A(\alpha, \beta, \gamma)\mathbf{R}_y(\theta_{YZ})^{-1}\mathbf{n}. \tag{43}$$

The generalized contact force $\mathbf{Q}_N$ is given by the sum of the contact forces normal to each contact surface integrated over the length of the element is

$$\mathbf{Q}_N = \sum \int_0^L \mathbf{S}(p)^T \mathbf{f}_N dp = \int_0^L \mathbf{S}(p)^T (\mathbf{f}_N^{s1} + \mathbf{f}_N^{s2} + \mathbf{f}_N^{w}) dp. \tag{44}$$

where the superscripts indicate the contact surface. A version of the sheave interaction described in this section was previously presented to examine dynamic contact due to wind induced vibrations for marine cranes [23]. In the next section, the implementation of the winch rotation using kinematic constraints is described.

2.5. Winch Rotation and Kinematic Constraint

The end of the cable is constrained to an arbitrary point on the surface of the winch, such that the rotation of the winch will reel the cable in or out. The augmented or Lagrange multiplier formulation [24] is used to define the generalized constraint force. In the augmented formulation, a force is applied to each constrained node in order to satisfy a constraint equation of the form

$$\mathbf{\Phi}(\mathbf{q}, t) = \mathbf{0} \tag{45}$$

at the acceleration level ($\ddot{\mathbf{\Phi}} = 0$). The force $\mathbf{Q}_c$ required to satisfy the constraint can then defined by introducing a vector of Lagrange multipliers λ:

$$\mathbf{Q}_c = -\mathbf{\Phi_q}^T \lambda. \tag{46}$$

The equations of motion for the constrained element becomes

$$\mathbf{M}\ddot{\mathbf{q}} - \mathbf{Q}_{ext} + \mathbf{Q}_{int} + \mathbf{\Phi_q}^T \lambda = \mathbf{0}. \tag{47}$$

Due to numerical error inherent to a non-ideal computational environment, Equation 45 can not be satisfied exactly resulting in the accumulation of error or "constraint drift." To compensate for the numerical error, Baumgarte's stabilization method [25, 26] is applied. In Baumgarte's method, the equation

$$\ddot{\mathbf{\Phi}} + 2a_1\dot{\mathbf{\Phi}} + a_2^2\mathbf{\Phi} = 0, \tag{48}$$

where a_1 and a_2 are chosen constants, is to be satisfied instead of the original constraint $\ddot{\mathbf{\Phi}} = 0$. The additional terms introduce feedback, similar to a PD controller, if the solution drifts from the constrained value. For $a_1 = a_2 > 0$, the solution is asymptotically stable [26].

Expanding the second time derivative of $\Phi(\mathbf{q}, t)$, Equation 48 can be expressed as

$$\mathbf{\Phi_q}\ddot{\mathbf{q}} = \mathbf{b} \tag{49}$$

where $\mathbf{\Phi_q}$ is the Jacobian of $\mathbf{\Phi}$ and $\mathbf{b}$ is a column vector given by

$$\mathbf{b} = -\mathbf{\Phi}_{tt} - (\mathbf{\Phi_q}\dot{\mathbf{q}})_{\mathbf{q}}\dot{\mathbf{q}} - 2(\mathbf{\Phi_q})_t\dot{\mathbf{q}} - 2a_1\dot{\mathbf{\Phi}} - a_2^2\mathbf{\Phi}. \tag{50}$$

Combining Equations 49 and 47, the Lagrange multipliers can be written

$$\lambda = \left[\mathbf{\Phi}_q\mathbf{M}^{-1}{\mathbf{\Phi}_q}^T\right]^+ (\mathbf{\Phi_q}\mathbf{a} - \mathbf{b}) \tag{51}$$

where $^+$ represents the Moore-Penrose pseudo-inverse and $\mathbf{a}$ is the associated accelerations of the unconstrained system

$$\mathbf{a} = \mathbf{M}^{-1}(\mathbf{Q}_{\text{ext}} - \mathbf{Q}_{\text{int}}) \tag{52}$$

The constraint forces can then be determined using Equation 46.

The constraint used in the current study consists of one end of the cable pinned to the surface of the winch. The motion of the pin joint incorporates the rigid body motion of the ship and the rotation of the winch about its axis and is defined by the equation

$$\mathbf{\Phi} = \mathbf{r}_0 - \mathbf{r}_{CG} - \mathbf{R}_B^I(\alpha, \beta, \gamma)(\mathbf{s}_w + \mathbf{R}_y(\phi)r_w\mathbf{k}) = 0 \tag{53}$$

where $\mathbf{r}_0$ is the position of the first node of the first element, $\mathbf{r}_{CG}$ is the position of the center of gravity of the ship, $\mathbf{s}_w$ is the position of the winch in the body-fixed coordinate frame, $\mathbf{R}_B^A$ is the rotation matrix from the ship's body frame to the absolute frame, $\mathbf{R}_y(\phi)$ is the rotation matrix corresponding to the rotation of the winch about its axis by an angle ϕ and $\mathbf{k} = [0 \quad 0 \quad 1]^T$ is a unit vector in the Z axis.

The winch rotation is used to implement motion compensation algorithms which serve to minimize the motion of the towbody by reeling the cable in and out based on the motion of the ship. An additional degree of freedom is added to the equations of motion representing the winch rotation ϕ. The acceleration of the winch is given by a PD control equation

$$\ddot{\phi} = k_1(\phi_{SP} - \phi) + k_2(\dot{\phi}_{SP} - \dot{\phi}) \tag{54}$$

where k_1 and k_2 are chosen constants and ϕ_{SP} is a set-point. The set-point algorithms examined in this study were developed by Calnan et al. [27, 28] and will be summarized in Section 3. In the next section, the computer implementation of the model is described.

2.6. Computer Implementation

The numerical simulation of the model was performed in MATLAB using the stiff ODE solver *ode15s*. Figure 7 shows a flowchart of the overall procedure. Prior to the simulation, the constant mass matrix $\mathbf{M}$ is computed using Equation 8 for each element. An initial vector of vertically concatenated element coordinates $\mathbf{q}$ is defined and input to the ODE solver. At each time step, the generalized elastic forces $\mathbf{Q}_e$ and damping forces $\mathbf{Q}_d$ are calculated using Equations 9 and 19. The external force distributions are calculated as described in Sections 2.2, 2.3, and 2.4 for a discrete set of points along each element. The equivalent generalized forces are then computed using the numerical quadrature defined in Equation 6. For the elements below the waterline the modified mass matrices are calculated using Equations 27 and 34. The element mass matrices are concatenated into a block diagonal matrix, while the generalized forces are concatenated vertically.

To enforce C^1 continuity of the cable profile, the generalized coordinates of adjacent nodes are made to be equal, resulting in an independent set and a dependent set of element coordinates. The system equations of motion can then be reduced to contain only the independent coordinates using the embedding procedure described by Shabana [24]. Next, the winch acceleration is determined via Equation 54 and the generalized constraint force needed to satisfy the kinematic constraint is determined using the process described in Section 2.4. Finally, Equation 4 is solved for the nodal accelerations $\ddot{\mathbf{q}}$ which are returned to the ODE solver.

In order to initialize the model, an initial set of generalized coordinates is generated. The initial configuration consists of a straight, undeformed cable tangent to the sheave surface. Using a spherical kinematic constraint, the end of the cable is constrained to move along a path tangent to the sheave and winch surfaces, coming to rest at a nominal position on the winch surface. The system is then allowed to reach steady state and the final vector of generalized coordinates is then stored, to be used during the final simulation.

The six axis ship motion is loaded as a time series. The MATLAB function *spapi* is then used to produce a third-order piece-wise polynomial fit of the data. As the ODE solver *ode15s* uses a variable time step, the piece-wise polynomial allows the ship position and rotations and their derivatives to be evaluated at any time t during the numerical integration. One will notice that model formulation and construction is independent of the ship dynamics, and thus the user is required to develop the time series of the ship motion either through numerical methods such as the Cummins equation [29], via experimentally validated software such as ShipMo3D [30] or from physical sensor data.

The following section describes the validation of the model using small scale experimental measurements is described.

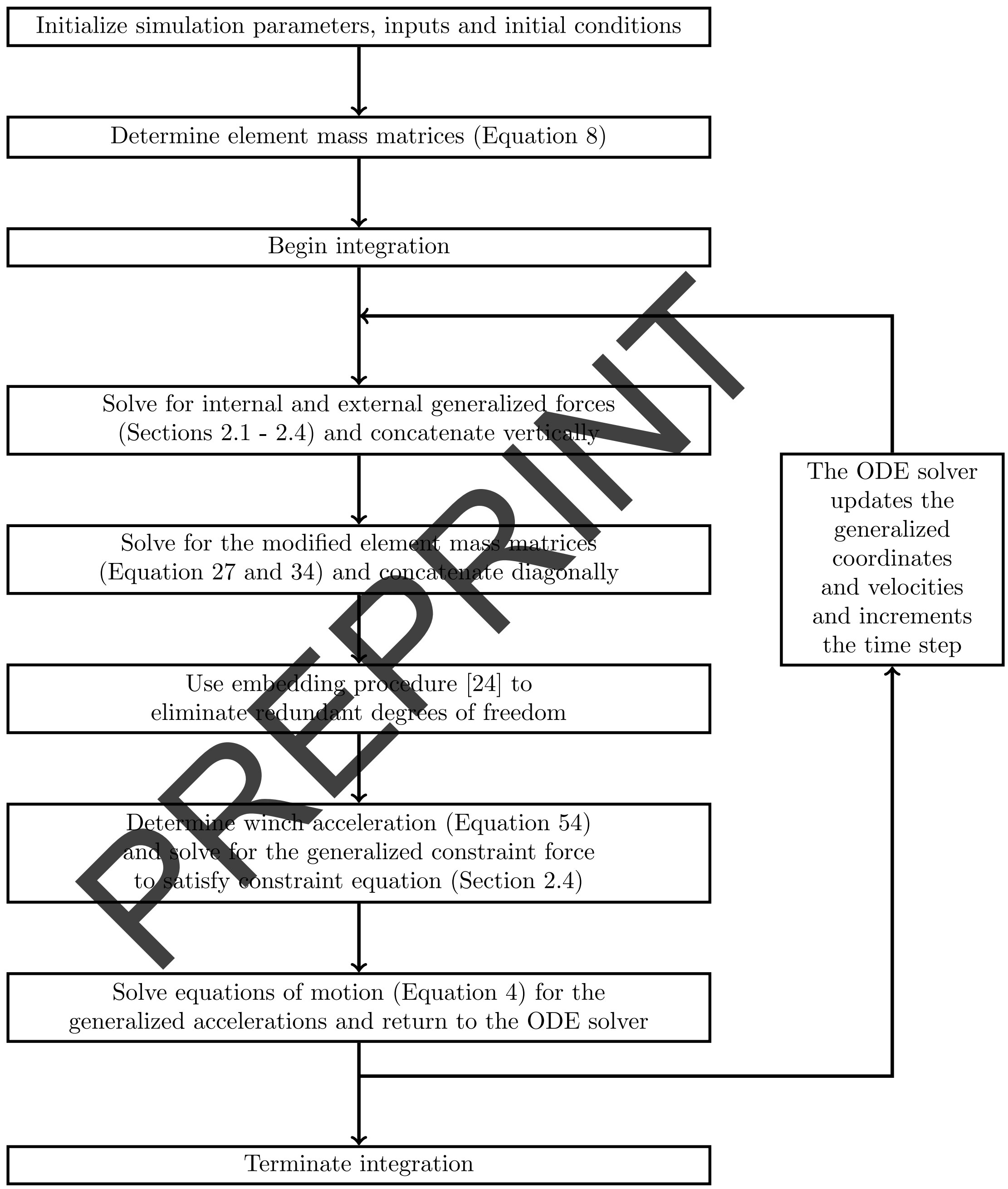

Figure 7: Flowchart of the simulation procedure.

3. Model Validation

In order to validate the model, the simulated cable behavior was compared to experimental measurements for small scale cable systems. Previously, a system consisting of a nylon rope running over a pulley and supporting a suspended load was considered [31, 32]. The load was given an initial deflection and allowed to swing. The resulting cable tension and wrap angle of the cable of the pulley were measured and compared to the simulated time series. Three cases with varying load mass and variations were examined. The motion was simulated for ten seconds. Good agreement between the simulation and experimental measurements was found. The standard deviation of the error between the simulated and measured wrap angle ranged from 1.37 to 3.73 degrees with peak-to-peak variations in the wrap angle up to 110 degrees. The standard error ranged from 6.2 to 14.6 N for the cable tension, with peak-to-peak variations up to 166 N.

Additional verification of the model implementation was performed by comparing the simulated output to experimental data obtained by Takehara et al. [33]. Takehara et al.'s experiment consisted of rubber tether submerged in still water. The left side of Figure 8 illustrates the three test cases that were performed, while the right side plots the error in the Euclidean position between the simulated cable motion and the Takehara et al. data at the midpoint and end of the tether for each case. In Cases 1 and 2, the tether was pinned at one end and released from a horizontal position. In Case 2, an additional spherical mass was attached at the mid point of the cable. In Case 3, the tether was suspended vertically and the pin joint was translated horizontally at a constant velocity. The tether was 0.8 m long with a diameter of 3.4 mm. A linear density of 1.273×10^{-2} kg/m and Young's modulus of 2.79×10^{7} Pa was used in the simulations. The spherical mass in Case 2 was 67.8 g and a diameter of 2.5 cm. In Case 3, the pin joint was translated at a velocity of 0.5 m/s for 1 s and then held fixed. The experimental data was extracted from the figures presented by Takehara et al. and compared with the simulated output of the model presented in Section 2. The simulation results demonstrate good agreement with the experimental data with RMS errors in the cable position, shown on the right side of Figure8, ranging from 5.8 mm to 48.5 mm. These errors are small relative to the overall cable length of 800 mm and are consistent with the simulated results obtained by Takehara et al. The largest RMS error was observed for Case 2 at the endpoint of the cable, however the position of the midpoint where the mass was attached was predicted more accurately with an RMS error of only 12.2 mm.

The main focus of this section is on the validation of the model for a towcable system which includes cable-winch contact and winch motion. The following sections discuss the validation of the model using previously recorded measurements of towbody motion in a flume tank.

3.1. Flume Tank Study Setup

Calnan et al. [27, 28] developed a number of Active Heave Compensation (AHC) algorithms, which serve to minimize the disturbance to the towbody as a result of the ship motion. The algorithms determine a winch rotation setpoint as a function of the ship displacement and the angle of the tow-cable as it exits the sheave. Calnan et al. also performed an experiment (hereafter referred to as the flume tank study) to quantify the efficacy of the AHC algorithms using a recirculating flume tank and a small scale winch system. Figure 9 shows a schematic of the system consisting of a three degree of freedom motion mechanism mounted above the flume tank. The motion mechanism is used to position a small cylindrical winch which is powered by a DC motor. A spherical towbody is attached to the winch by a thin nylon cable; the system did not include a sheave. The top of the winch in its nominal position was located 46 cm above the waterline. Table 1 lists the parameters of the flume scale experiment. Note that the cable length is measured from the top of the winch. With a steady flow in the flume tank, video recordings of the towbody motion were taken using two cameras, one perpendicular to the flow and one facing in the direction of the flow and submerged in the flume tank. The two videos were

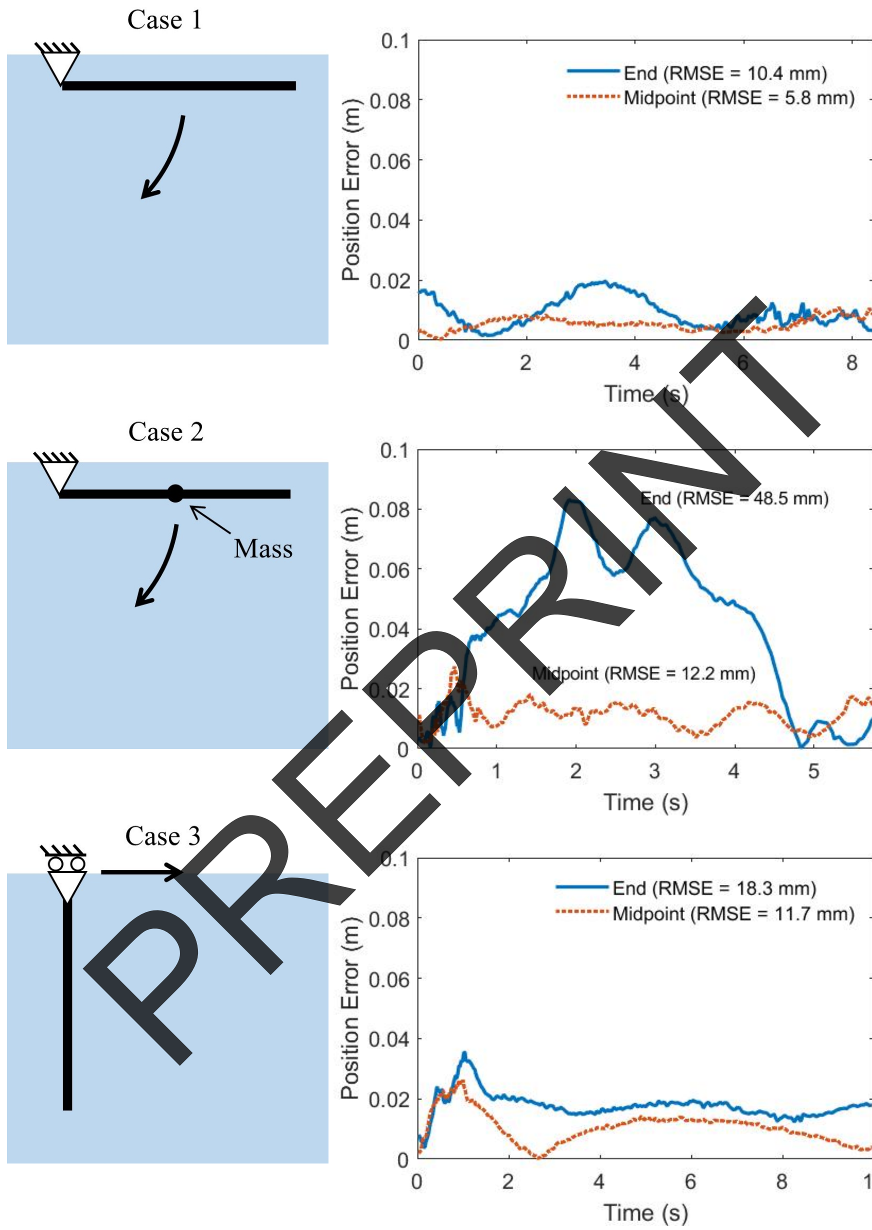

Figure 8: Diagrams of test cases performed by Takehara et al. [33]. Cases 1 and 2 consist of a falling tether pinned at one end with a spherical mass attached at the midpoint in Case 2. Case 3 consists of a hanging tether with a moving support. Plots of the error in the Euclidean position of the end and midpoint of the tether between the experimental data and the simulated results are shown to the right of each diagram.

used to produce a three dimensional trace of the towbody motion. Example frames of the videos captured by the two cameras are shown in Figure 9.

Additionally, Calnan et al. developed a simulation of the cable motion using rigid linear elements, also known as the finite segment method (FSM). The ANCF cable model developed in the current study was used to simulate the towbody motion based on the winch motion and system parameters from the previous flume tank study [27, 28]. The simulated motion from the ANCF model was then compared with the experimental data and simulated motion from the FSM model. Four cases were considered, including two motion compensation algorithms:

1. No winch motion
2. Winch motion without compensation
3. Winch motion with compensation (simplified sheave algorithm)
4. Winch motion with compensation (rigorous sheave algorithm)

In the rigorous case, the angle of the cable at the sheave can be measured directly, whereas in the simplified case a nominal value of the angle is assumed. Two other algorithms, referred to as rigorous waterline and simplified waterline, demonstrated poor performance and unreliability in the flume tank study and were thus not examined in the current study.

Parameter	Value
Cable diameter	0.45 mm
Linear cable density	0.2 g/m
Nominal cable length	1.01 m
Sphere diameter	10 mm
Sphere mass	1.33 g
Water density	1026 kg/m^3
Water viscosity	1.2×10^{-3} Pa·s
Mean surface velocity	0.330 m/s
Winch radius	17.35 mm

Table 1: Flume scale system parameters [27, 28].

The ship motion used to validate the FSM and ANCF models is data digitized from an Australian Defence Science and Technology Organisation (DSTO)

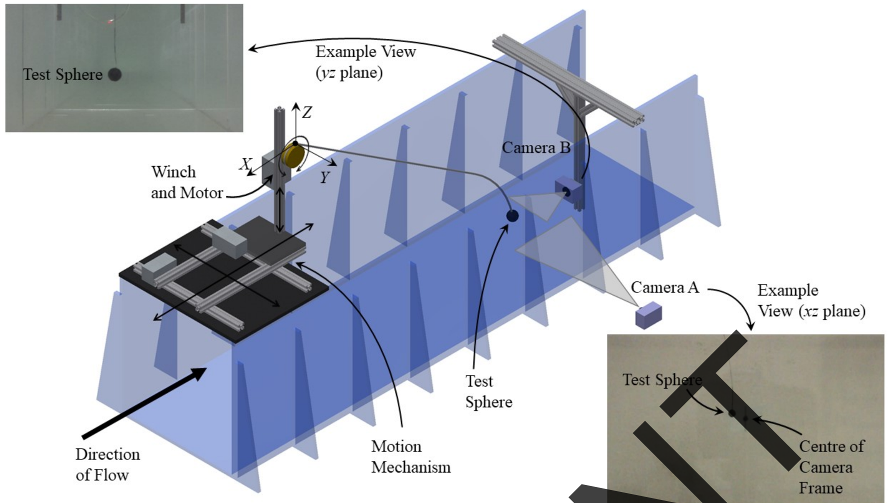

Figure 9: Illustration of the flume tank system and experimental apparatus. The origin of the absolute frame is located at the top of winch in its nominal position. The example views show sample images from the two orthogonal cameras.

report [34]. The data was used to determine the 3 degree-of-freedom translational motion of a winch located at the ship's stern and was then scaled to fit within the flume tank environment. Figure 10 shows the displacement of the winch along each axis as a function of time.

Additionally, measurements of the flow velocity at several depths below the surface of the water were taken. A empirical linear relationship between the mean flow velocity $\overline{\mathbf{V}}_f$ and depth was found to be

$$\overline{\mathbf{V}}_f = (-0.5873 \text{ 1/s})(z - z_{WL}) - 0.3302 \text{ m/s} \tag{55}$$

where z is the vertical position in the absolute frame and z_{WL} is the position of the waterline in meters. The standard deviations of the flow along the x, y and z axes were found to be 0.0300 m/s, 0.0262 m/s, and 0.0152 m/s, respectively. A Chebyshev II low-pass filter with 80dB attenuation was to a white noise signal in order to approximate the frequency spectrum of the measured velocity and scaled the filtered signal to match the measured variances in each axis [35]. The Chebyshev II filter was used in the current study to generate a time series of

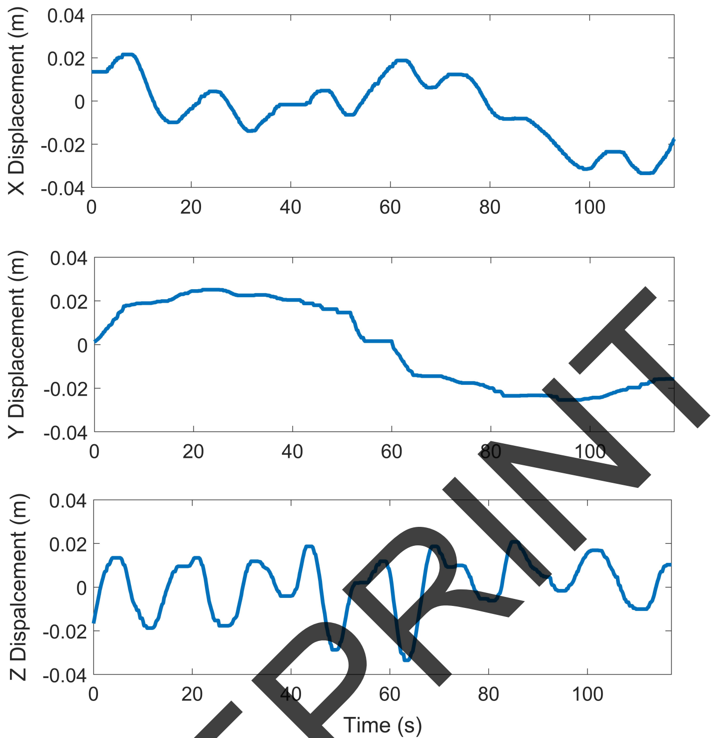

Figure 10: Winch displacement as a function of time from Calnan's flume tank experiment [35].

the flow velocity at a frequency of 100 Hz prior to the simulation.

In the flume-scale study, a state-space model of a DC motor with position control was used to convert the PD controller output to a rotational acceleration [28]. The PD gains were tuned based to obtain a 90% rise time of 0.2 s in response to a step input of 0.5764 rad. The length of cable reeled in or out by the winch tracked the AHC set point to within 1 mm for the majority of the motion. In the current study, the system was simplified such that the angular acceleration is given directly by the PD output of Equation 54. The proportional and derivative gains k_1 and k_2 were tuned to obtain tracking errors within 1mm and a 90% rise time of 0.2s. The proportional and derivative gains were selected to be 200 and 20, respectively.

The added mass coefficients of the cable and the towed sphere C_m and $C_{m,b}$ were selected based on theoretical values of 1 and 0.5 [36], respectively, which are consistent with the previous values [35]. The hydrodynamic loading functions f_n and f_t of Equation 22 corresponding to a bare cable are

$$f_n = 0.5 - 0.1 \cos \eta + 0.1 \sin \eta - 0.4 \cos 2\eta - 0.11 \sin 2\eta \tag{56a}$$

$$f_t = 0.01 \left(2.009 - 0.386\eta + 1.9159\eta^2 - 4.162\eta^3 + 3.506\eta^4 - 1.187\eta^5\right) \tag{56b}$$

where η is the angle of attack between the cable and the flow [16]. The following additional parameters were identified using the ANCF cable model: cable bending stiffness EI, damping coefficient c and drag amplification factor G. The estimation of these parameters is described in the following section. Additionally, a convergence study was performed to ensure the accuracy of the simulations.

3.2. Parameter Estimation

The cable used in the flume tank tests was a nylon monofilament [35]. The previous work [28, 35] assumed an elastic modulus E of 3 GPa, however reported values of the elastic modulus for Nylon 6-6, a material commonly used in these lines, range from 0.7 to 5 GPa [37]. It is therefore necessary to estimate the bending stiffness empirically to avoid unrealistic curvature at the winch transition.

A test was conducted to approximate the elastic modulus using the same cable used in the initial experiment performed by Calnan et al. The test consisted of clamping one end of a small length of the cable horizontally with a spherical mass attached at the free end. The cable had a length of 46.4 mm measured from the fixed point to the center of the sphere. A photograph, Figure 11 was taken of the cable profile in front of a grid of known spacing. Twenty-five points, indicated by red circles, were selected graphically on the photograph and converted from pixel coordinates to spatial coordinates based on the grid spacing. The points were then be compared to the simulated cable profile.

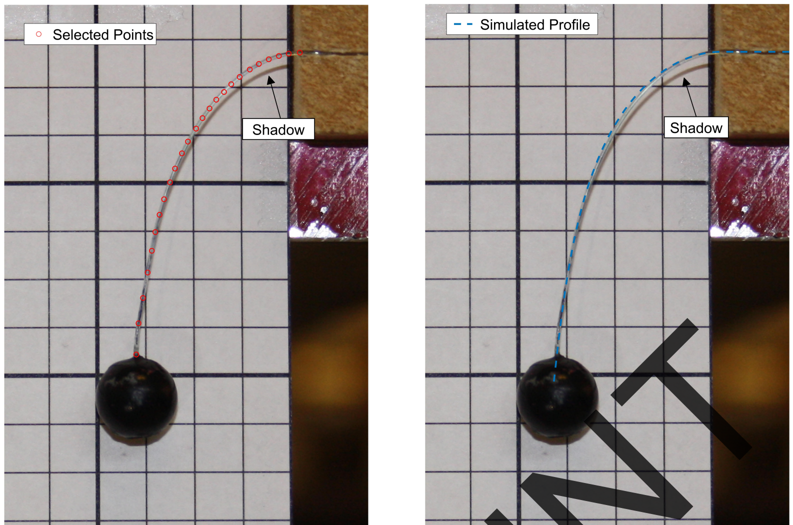

Figure 11: Photograph of clamped cable with manually selected points (left) and simulated cable profile (right).

A golden section search over a range of $E = 2 \times 10^{-6}$ Nm^2 to 6×10^{-6} Nm^2 was used to minimize the sum of the squared distance between each point and the simulated profile. Twenty cable elements were used to determine the profile of the cable at equilibrium. The optimal value of E found by the search was 1.40 GPa. Figure 11 shows the final simulated cable profile as a blue line overlaid on the photograph on the right.

In order to determine an appropriate damping coefficient c of Equation 19 for the current study, a simplified model was introduced to approximate the relationship between the intrinsic damping and the damping coefficient. The simplified system consists of a vertical cable clamped at the top. The bottom of the cable is free and attached to a lumped mass. The cable and mass properties were kept the same as the parameters of the flume tank experiment listed in Table 1. The cable was deflected a small amount and then released. The damping ratio ζ is determined from the amplitude of successive peaks in the horizontal displacement. The observed damping ratio was determined for a range of damping coefficients from 1×10^{-4} to 10×10^{-4} Ns. The damping ratio

ζ and damping coefficient c were found to have a linear relationship over the range. The equation of the line of best fit was determined to be $\zeta = 112.72c$ ($R^2 = 1$). Based on the damping ratio of 0.061 determined experimentally by Calnan [35], the damping coefficient was selected to be $5.4{\times}10^{-4}$ Ns.

The drag amplification due to vortex shedding is quantified in the model by the amplification factor G of Equation 24. This parameter was tuned based on the mean tow body position recorded in the flume tank experiments with a steady flow in the flume and no motion applied to the winch. The centroid of the experimental towbody motion was $[-0.708, -0.008, -0.685]$ m. The steady state position of the was obtained by running the simulation with no noise or winch motion. The system was considered to have reached equilibrium when the maximum velocity of any point on the cable is less than 1×10^{-4} m/s. The error was taken as the Euclidean distance between the steady-state towbody position and the centroid of the experimental data. The amplification factor was estimated using a golden-section search method over a range from 1 to 2. The identified value of the amplification factor G was 1.737 with an error of 5.0 mm. Having determined the model parameters, the number of ANCF elements in the cable mesh is examined in the following section.

3.3. Cable Mesh

Since the elements in contact with the winch will have a much larger curvature than the rest of the cable, it is desirable to use a variable mesh such that smaller elements are used for the contact region and larger elements are used elsewhere. A variable mesh will minimize the number of elements required to obtain convergence and thereby reduce the computational requirements of the simulation.

The cable is thus divided into two segments with segment 1 comprising all points on the cable that may come into contact with with winch surface throughout the motion and segment 2 comprising the remaining length of cable. Figure 12 illustrates the two segments. The lengths of the two segments and the nominal angle of rotation of the winch ϕ_{nom} measured from the vertical axis were selected to give a cable length of 1.01 m measured the top of the winch when the winch is in its nominal position. The selected segment lengths were 81.8 mm and 955.5 mm and the nominal winch rotation was 1.57 rad.

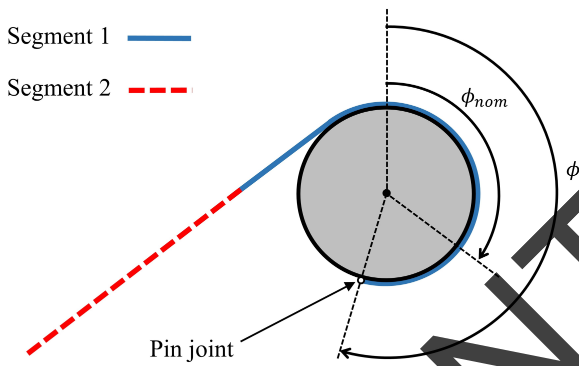

Figure 12: Cable segments and winch rotation.

Next, a convergence study was performed by successively increasing the number of elements in the two sections. The mesh for segment 1 was refined first, keeping the number of elements in segment 2 constant at 4 elements. Simulations were performed using the simplified sheave algorithm for 20 seconds with the number of elements in the first segment ranging from 4 to 16. Table 2 lists the computation time for each simulation as well as the mean absolute error (MAE) in the towbody position relative to the most refined mesh. The change in the tow body motion was found to be insignificant between the 12 element and 16 element simulations with a mean difference of 0.156 mm. Thus 12 elements was selected for the first segment. The mesh for the second segment was then refined, keeping the number of elements in the first segment constant at 12 elements. Again, 20 s simulations were performed with the number of elements ranging from 4 to 16. Referring to Table 3, the change in the towbody motion was again found to be insignificant between the 12 element and 16 element simulations with a mean difference of 0.05 mm. Twelve elements was selected for the second segment.

Number of Elements	4	8	12*	16
MAE in towbody position (mm)	3.310	0.615	0.156	–
Computation time (min)	11.7	14.4	16.7	18.4

* Selected value for flume-scale simulation

Table 2: Convergence results for segment 1

Number of Elements	4	8	12*	16
MAE in towbody position (mm)	0.442	0.131	0.048	–
Computation time (min)	16.7	21.9	26.5	29.7

* Selected value for flume-scale simulation

Table 3: Convergence results for segment 2

3.4. Test Cases and Results

For each simulation, an ellipsoid was fit to the trace of the towbody motion such that it contained 95% of the data points. Calnan's ellipsoid fitting algorithm was used to fit the ellipsoid to the data. Figure 13 illustrates the principal axes of the ellipsoid X_E, Y_E and Z_E. The ellipsoid fitting algorithm consists of centering the ellipsoid coordinate frame at the centroid of the simulated data. A best fit line and best fit plane are then fit to the data. The ellipsoid frame is rotated such that the X_E axis is aligned with the best fit line and the X_E and Y_E axes are coplanar with the best fit plane. The radii of the ellipsoid are scaled proportional to the variance along each axis until 95% of the points are contained within the volume.

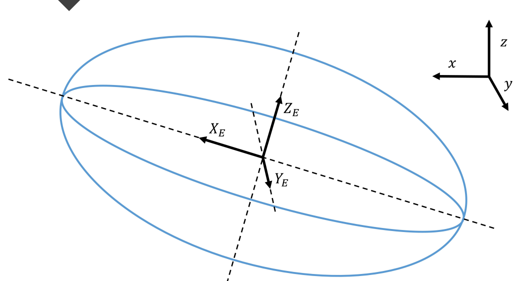

Figure 13: Ellipsoid principal axes and absolute coordinate frame.

The simulation was first performed without motion of the winch and the motion of the towbody was determined. Figure 14 shows the simulated towbody motion as a blue line viewed from the side of the flume tank, while the experimental body motion is plotted as an orange line and the towbody motion simulated using the FSM model as a yellow line. Table 4 gives the results of the ellipsoid fitting and the standard deviation of the motion along each ellipsoid axis. The percent errors compared to the experimental results are given in parentheses. While the FSM simulation underpredicted the ellipsoid volume by 58%, the current ANCF simulation overpredicted the volume by a similar amount. The ANCF simulation better predicted the centroid of the towbody motion. The distance between the centroid of the experimental motion and the simulation motion was 0.48 cm for the ANCF simulation and 1.59 cm for the FSM simulation. In this test case, the motion of the towbody is due entirely to variations in the flow velocity, which can not be accurately captured by the model. These variations are significant at small scale, but are not expected to significant for a full scale system.

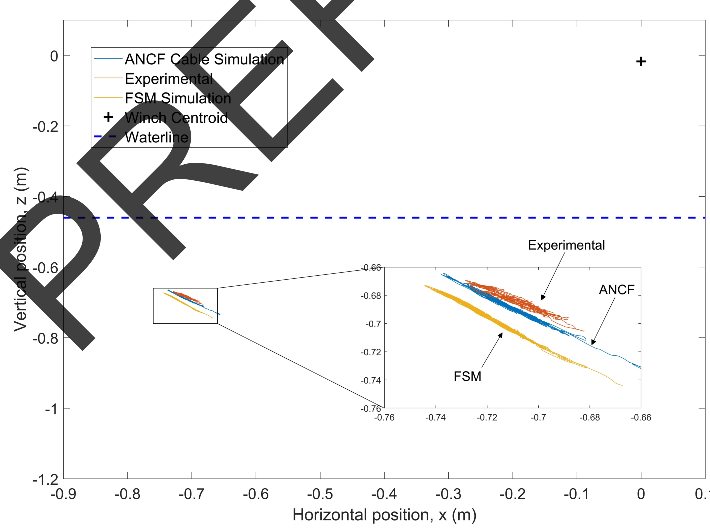

Figure 14: Motion of towed sphere with no winch motion.

Next, the simulation was first performed with winch motion but without heave compensation. Table 5 compares the ellipsoid fitting results for the sim-

	Experimental	FSM Sim.	ANCF Sim.
Ellipsoid Volume (cm^3)	4.82	2.04 (-58%)	7.76 (61%)
X_E Std. Dev. (cm)	1.19	1.43 (20%)	1.56 (31%)
Y_E Std. Dev. (cm)	0.78	0.43 (-45%)	1.23 (58%)
Z_E Std. Dev. (cm)	0.13	0.05 (-62%)	0.07 (-49%)

Table 4: Results for no winch motion test case. Error relative to experimental values in parentheses.

ulated and experimental motion. The ANCF simulation agreed closely with experimental ellipsoid volume with an error of only 1.7%, a significant improvement over the FSM simulation which had an error of -24%. Again, an improvement was seen in the location of centroid of the towbody motion. The distance between the centroid of the experimental motion and the simulation motion was 2.15 cm for the ANCF simulation and 3.25 cm for the FSM simulation.

	Experimental	FSM Sim.	ANCF Sim.
Ellipsoid Volume (cm^3)	182.84	138.51 (-24%)	185.96 (1.7%)
X_E Std. Dev. (cm)	2.73	2.20 (-20%)	2.14 (-21%)
Y_E Std. Dev. (cm)	1.36	1.41 (3.8%)	1.55 (14%)
Z_E Std. Dev. (cm)	0.88	1.04 (19%)	0.97 (10%)

Table 5: Results for uncompensated case with winch motion. Error relative to experimental values in parentheses.

Finally, the motion was simulated utilizing the rigorous sheave and simplified sheave heave compensation algorithms. Figure 15 shows the towbody motion for the rigorous sheave test case. Tables 6 and 7 give the ellipsoid fitting results for the simplified and rigorous sheave test cases, respectively. In both cases the ellipsoid volume predicted by the ANCF simulation was smaller than the experimental volume, but a significant improvement over the FSM simulation was observed. For the simplified sheave case, the ellipsoid volume was 27% smaller for the ANCF simulation and 51% smaller for the FSM simulation. For the rigorous sheave case the volume was 22% smaller for the ANCF simulation and 56% smaller for the FSM simulation. The standard deviation of the motion along the Z_E axis of the ellipsoid was significantly smaller in the simulation than in the experimental results for both simulations.

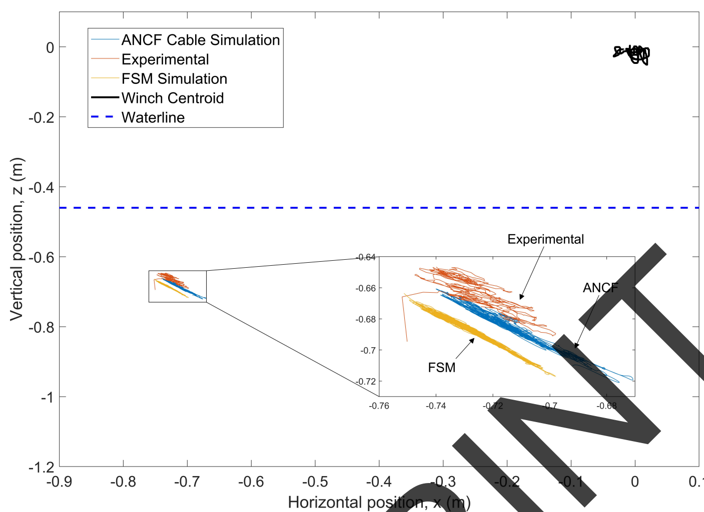

Figure 15: Motion of towed sphere for rigorous sheave test case.

	Experimental	FSM Sim.	ANCF Sim.
Ellipsoid Volume (cm^3)	36.55	18.00 (-51%)	26.68 (-27%)
X_E Std. Dev. (cm)	2.58	2.07 (-20%)	2.82 (9%)
Y_E Std. Dev. (cm)	1.29	1.18 (-8.5%)	1.67 (30%)
Z_E Std. Dev. (cm)	0.28	0.13 (-52.5%)	0.12 (-58%)

Table 6: Results for simplified sheave case. Error relative to experimental values in parentheses.

	Experimental	FSM Sim.	ANCF Sim.
Ellipsoid Volume (cm^3)	24.92	11.07 (-56%)	19.55 (-22%)
X_E Std. Dev. (cm)	2.42	2.08 (-13.9%)	2.42 (0.3%)
Y_E Std. Dev. (cm)	1.15	1.14 (-1.2%)	1.48 (28%)
Z_E Std. Dev. (cm)	0.28	0.06 (-78%)	0.10 (-66%)

Table 7: Results for rigorous sheave case. Error relative to experimental values in parentheses.

The ANCF simulations and the FSM simulations showed similar errors in the centroid of the motion in both cases. For the simplified sheave case, the distance between the centroid of the experimental motion and the simulation motion was 1.88 cm for the ANCF simulation and 2.14 cm for the FSM simulation. In the rigorous sheave case, the distance between the centroid of the experimental motion and the simulation motion was 2.62 cm for the ANCF simulation and 2.32 cm for the FSM simulation.

In general, the ANCF simulation performed significantly better at predicting the ellipsoid volume than the FSM simulation. Also, the ANCF simulation demonstrated less error in the location of the centroid of the motion for most test cases. The ANCF performed best for the uncompensated case, with an error in the ellipsoid volume of only 1.7%. The highest error was observed in the case with no motion, with an error of 61%. One possible source of error in the simulations can be attributed to the fact that the noise component of the flow velocity is the same at every point in the tank at a given time. Only the mean component of the flow was varied as a function of depth. In reality, the turbulence in the flow velocity is not uniform throughout the tank. This source of error is likely to be most significant in the case with no winch motion, as the motion of the towbody is governed only by the variation in the flow.

In the next section, a case study of a full-scale sheave and winch system is described which highlights the dynamic cable-sheave interaction.

4. Full Scale Simulation and Case Study

To demonstrate the capabilities of the techniques outlined in this paper for a full scale system, a case study was performed. The system consists of a towbody connected to the vessel by a wire rope, as illustrated in Figure 1. In this case study an overboarding sheave is considered. Table 8 lists the system parameters used in the simulations. For a 30m test vessel, the ship motion was generated using the experimentally validated ShipMo3D software package [30, 38], which has also been used in NATO studies [39]. The wave conditions were modelled using a unidirectional Bretschneider spectrum with a significant wave height of 3.25 m and a peak wave period of 9.7 s. Twelve test cases consisting of various headings and ship speeds were used. The conditions at which cable detachment are likely to occur were then determined.

Parameter	**Value**
Cable Diameter	10 mm
Cable Mass per unit length	0.389 kg/m
Cable length (nominal)	450 m
Towbody net weight	445 N
Towbody mass	250 kg
Sheave radius	0.25 m
Sheave groove depth	10 mm [40]
Sheave throat angle	60° [40]
Winch radius	0.30 m
Sheave position relative to ship CG	[-15, 0, 3.5] m
Winch position relative to ship CG	[-12, 0, 3] m

Table 8: Full scale system parameters.

The length of the cable is 105m and consists of steel wire rope with hard streamlined fairings attached. Hard fairings serve to reduce the drag force acting on the cable, thereby increasing the depth of the towbody and also having the effect of reducing the cable tension. For cables with hard fairings, the emprical loading functions f_n and f_t of Equation 22 are

$$f_n = -1.572 + 1.737\cos\eta + 2.407\sin\eta - 0.165\cos 2\eta - 0.781\sin 2\eta \tag{57a}$$

$$f_t = -0.116 + 0.464\cos\eta + 0.116\sin\eta \tag{57b}$$

where η is the angle of attack between the cable and the flow [41]. These loading functions are based on a constant drag coefficient C_D of 0.25.

The towbody consists of a cylindrical shell with a hydrofoil attached which produces a downwards force. The cylindrical shell and hydrofoil are treated independently for the purposes of determining the drag force coefficient and interference drag between the bodies is neglected. It is also assumed that the orientation of the body is constant throughout the motion and the axis of the cylindrical shell is align with the flow along the x-axis of the absolute coordinate frame. The cylindrical shell has a diameter of 300 mm and a length of 3 m. For axial flow along the horizontal x-axis the drag coefficient for a blunt cylinder is 0.85 [42]. For flow normal to the cylinder, along the y and z-axes, the drag coefficient is 1 [43]. For the hydrofoil, a NACA2412 cross-section with an area of 0.5 m^2 and angle-of-attack of -6° is assumed. For flow along the vertical z-axis, the hydrofoil is treated as a flat plate with a drag coefficient of 1.17 [42]. For flow along the x-axis, the drag coefficient of the wing is 0.008 [43]. The drag on the hydrofoil is assumed to be negligible for flow along the y-axis. The lift acting on the hydrofoil is calculated using a lift coefficient of -0.6 [43], giving a lift force of -722 N at steady state. An added mass coefficient of 1, based on the strip theory solution for a cylinder in normal flow [44], is used for accelerations along the y and z-axes. Added mass along the axis of the towbody is neglected.

An experiment by Ramberg and Griffin [45] examined the internal damping of marine cables and showed that their is an inverse relationship between cable tension and the damping ratio. Damping ratios for wire ropes can range from less than 0.1% when under tension [46] up to 37% for slack cables [47]. A damping ratio of 10% was assumed for this principal simulations documented in Section 4.2. Additionally, the effect of varying the damping ratio on the cable behavior will be examined. The relationship between the damping coefficient c and the damping ratio ξ was estimated using the same process described in Section 3.2 for the flume scale system. The relationship was found to be $c = 1.196 \times 10^3 \xi$ ($R^2 = 1$).

4.1. Convergence Analysis

To ensure that the selected mesh size would provide accurate results, a convergence study was performed. The cable was first divided into two segments to allow for the mesh size for the region in contact with the sheave and winch and the region submerged behind the vessel to be selected separately. A more refined mesh can thus be used in the contact regions to ensure that the contact forces are calculated accurately, while larger elements can be used elsewhere, in order to provide a reasonable computational efficiency. Figure 16 illustrates the two cable segments, where segment 1 has a length of 5m and segment 2 has a length of 100m.

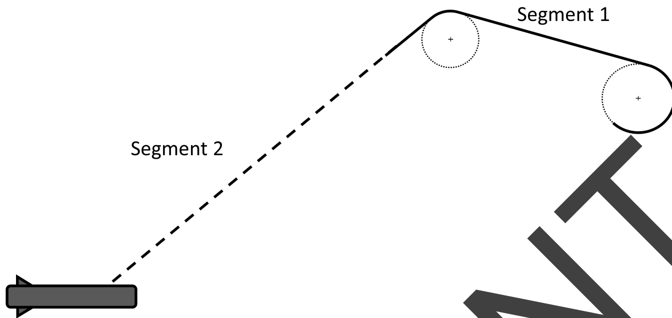

Figure 16: Cable segments for full scale simulation

The number of elements in segment 2 was varied first with the elements in segment 1 held constant at 10. Table 9 gives the mean cable tension for each mesh configuration as well as the computation time to simulate 30 seconds of motion. For each configuration, the cable tension time series was compared to the time series for the 30 element configuration and the mean absolute error between the two was calculated. From these results, it is observed that increasing the number of elements from 8 to 30 results in a mean change of only 1.26 N, but a 54% increase in the computation time. As this change is insignificant compared to the mean cable tension, 8 elements are used in the final simulations. The process was repeated for segment 1, the portion of cable in contact with the sheave and winch. In addition to the change in tension, the change in the contact force between the cable and the sheave was examined. In order to quantify an "overall" contact force magnitude, the norm of the contact force vector is integrated over the length of the element and then summed for each element making up the cable:

$$\mathbf{F}_{contact} = \sum_{i \in \{1,2,\ldots,N_e\}} \int_0^L ||\mathbf{f}_N(p)||dp, \tag{58}$$

where N_e is the total number of elements. The results for segment 1 are shown in Table 10. Very little change in the tension is observed. Increasing the number of elements from 60 to 100 results in a mean change of 12.1N, which is less than 1% of the average contact force over the 30s interval, but results in a significant increase (58%) in computation time. Thus, 60 elements were used in the final simulations.

Number of elements	2	4	6	8*	10	20	30
Mean Tension (N)	1682	1671	1667	1664	1662	1662	1663
MAE in Tension (N)	19.63	9.04	4.03	1.26	0.70	1.18	–
Comp. Time (s)	921	966	1007	1025	1029	1255	1583

* Selected value for full scale simulation

Table 9: Convergence results for segment 2

Number of elements	20	40	60*	80	100
Mean Tension (N)	1661	1661	1661	1661	1661
MAE in Tension (N)	0.257	0.084	0.022	0.012	–
Mean Contact Force (N)	1869	1867	1858	1851	1846
MAE in Contact Force (N)	33.8	23.8	12.1	4.8	–
Computation Time (s)	1342	1730	2289	2796	3616

* Selected value for full scale simulation

Table 10: Convergence results for segment 1

4.2. Results

The cable motion was simulated for a total of 12 test cases with ship speeds of 6, 8 and 10 knots and various ship headings relative to the wave direction. For each case, the motion was simulated for 60s. The time series of cable tension at the sheave was then calculated for each case. Additionally, it was determined whether or not the cable detached from the sheave by observing if the overall contact force given by Equation 58 reached a value of zero during the simulation. Table 11 summarizes the results.

Cable detachment was observed in only one test case: Run 2. Figure 17 shows the time series of the contact force for Run 2. Detachment, in which the contact force disappears, is observed at 32.3 s. Figure 18 is a graphical repre-

Run	1	2	3	4	5	6
Ship Velocity (knots)	6	6	6	6	8	8
Ship Heading (degrees)	30	60	120	165	30	60
Minimum Tension (kN)	0.263	0.026	0.921	1.163	0.693	0.252
Mean Tension (kN)	1.711	1.660	1.658	1.621	2.034	2.040
Maximum Tension (kN)	4.642	4.245	2.518	2.043	3.909	4.037
Detachment	No	Yes	No	No	No	No
Run	7	8	9	10	11	12
Ship Velocity (knots)	8	8	10	10	10	10
Ship Heading (degrees)	120	165	30	60	120	165
Minimum Tension (kN)	1.544	1.736	1.145	1.295	2.118	2.101
Mean Tension (kN)	2.000	1.981	2.577	2.557	2.521	2.556
Maximum Tension (kN)	2.577	2.170	4.022	4.290	2.923	3.066
Detachment	No	No	No	No	No	No

Table 11: Results of full scale simulations

sentation of the cable and winch during Run 2 and illustrates the detachment as a function of time. A main limitation of these results is that only 60 seconds of motion was simulated for each case, which may not represent the worst possible ship motion under the conditions examined in the twelve test cases.

Since there is a great deal of uncertainty regarding the internal damping ratio of the cable, which is largely dependent on the cable tension, additional simulations were performed with different damping ratios. Damping ratios of 2.5, 5, 10 and 20% were used and the ship motion was consistent with Run 2 from Table 11. Table 12 summarizes the results for each case. Detachment is observed with damping ratios of 10 and 20%. As the damping ratio is increased, the observed minimum tension decreases, thus increasing the likelihood of detachment. As noted before, the damping ratio increases with decreasing tension. This relationship between the tension and damping is likely to exacerbate the occurrence of cable detachment, and is thus an important area of interest for future work.

The conditions considered in this study—a small vessel in rough seas—represent a very severe case. Detachment of the cable from the sheave is thus unlikely during most towing operations when the body is at depth. The likelihood of detachment would be more significant during the launch and recovery

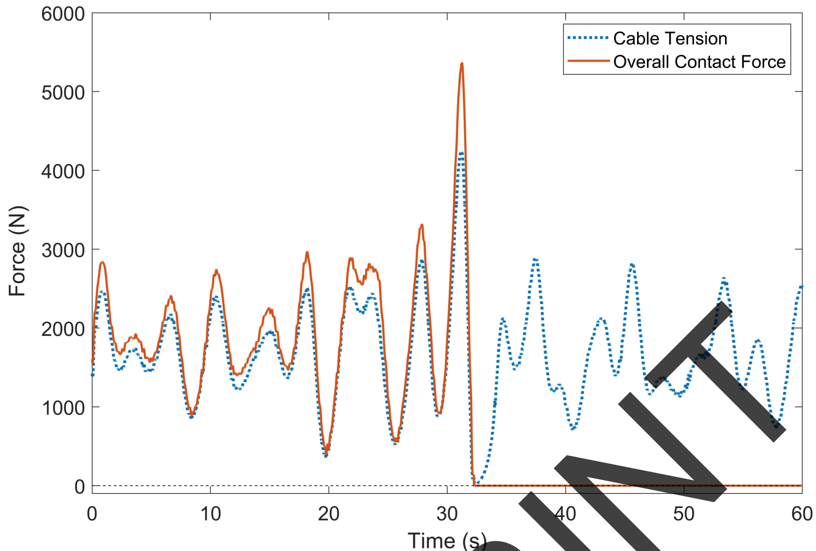

Figure 17: Cable tension and contact force as a function of time for Run 2.

Damping Ratio	2.5%	5%	10%	20%
Minimum Tension (kN)	0.114	0.057	0.026	-0.007
Mean Tension (kN)	1.673	1.673	1.660	1.645
Maximum Tension (kN)	4.215	4.215	4.245	4.211
Detachment	No	No	Yes	Yes

Table 12: Results of full scale simulations with damping ratio varied.

stage, when the length of cable payed out is small. With a short length of cable the total drag acting on the cable and therefor the cable tension are significantly reduced. Additionally, reeling out the cable would cause the cable to slacken, which may lead to detachment. Actuation of the winch when applying motion compensation may also influence the variations in tension. Motion compensation was not examined in this study as the low tension and high damping caused the cable to exhibit undesirable rotations at the pin joint connecting the cable to the winch drum. A more accurate model of the cable-winch interaction—one which incorporates the tangential friction forces and pretensioning of the cable—is required in order to accurately model the cable behavior with motion compensation.

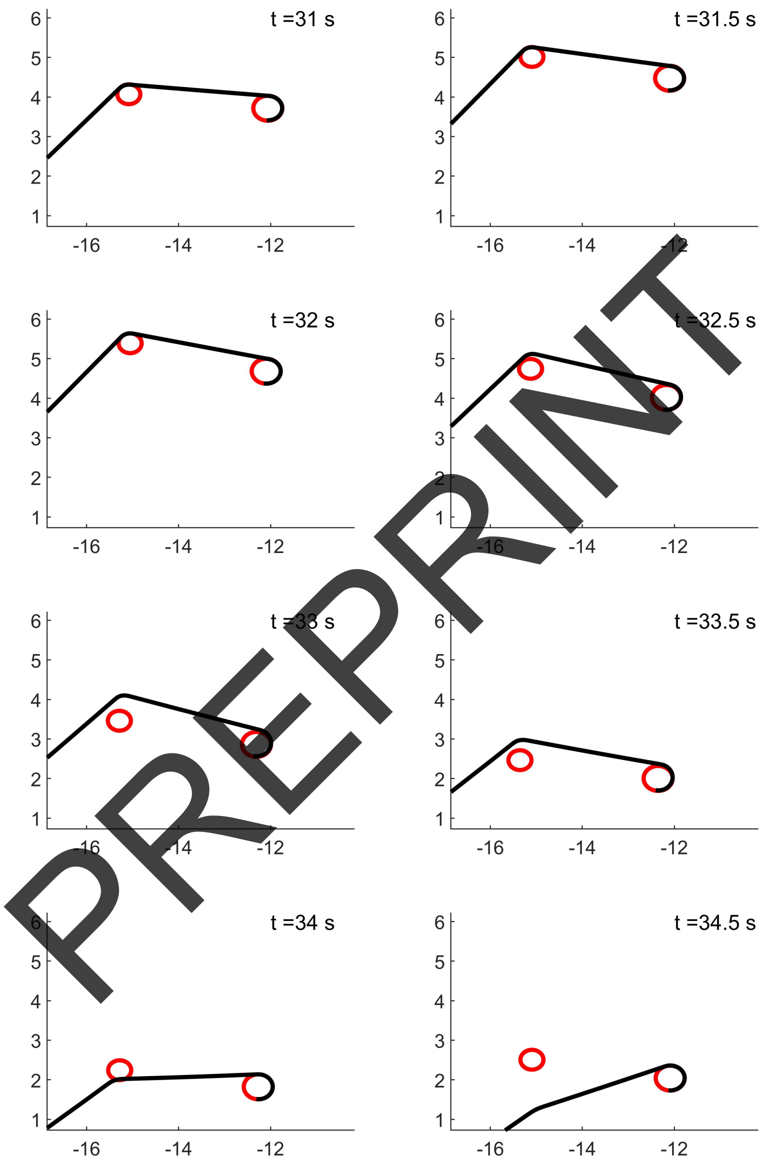

Figure 18: Graphical depiction of cable detachment for Run 2. The sheave and winch are depicted as red circles. Axes are in meters.

5. Conclusion

In this work, a finite element model of a towed cable system with dynamic cable-sheave and cable-winch interactions was presented. The Absolute Nodal Coordinate Formulation was utilized for modelling the cable elements and a contact penalty approach was used to describe the contact forces. A novel three-dimensional formulation of the contact between the cable and sheave groove was shown. Additionally, the model incorporates hydrodynamic drag and added mass and internal cable damping.

The performance of the simulation at predicting the towbody motion was assessed based on existing small-scale data. The ANCF simulation was compared both with the experimental towbody motion and the results of a previous Finite Segment Method (FSM) simulation. The ANCF model demonstrated good agreement with the experimental motion, predicting the volume of the enclosing ellipsoid to within 2% for the un-compensated case and within 27% for the cases with motion compensation. The ANCF model also demonstrated a significant improvement over the FSM model. Finally, a case study was conducted to examine the behavior of the model at full scale and to demonstrate dynamic contact behavior between the cable and sheave, including detachment of the cable from the sheave, during towing operations. Twelve test cases were considered and detachment was observed in one case.

Future work is suggested to address the variation of cable damping with tension. Additionally, the simulation may be further developed to examine the potential for cable detachment during launch and recovery. A more complex cable-winch interaction which incorporates the tangential contact forces is also needed in order to accurately model the cable behavior with motion compensation. Finally, additional validation of the model may be performed at full scale using measurements of the towbody motion and cable tension during a towing operation.

Acknowledgements

For their financial support, the authors would like to thank the Natural Sciences and Engineering Research Council of Canada (NSERC) and Kraken Robotic Systems Inc. The authors would also like to thank DSA LTD (Dynamic Systems Analysis Ltd) for the in-kind donation of ShipMo3D.

References

[1] Takehara S, Terumichi Y, Sogabe K. Motion of a submerged tether subject to large deformations and displacements. Journal of System Design and Dynamics. 2011;5(2):296–305.

[2] Park J, Kim N. Dynamics modeling of a semi-submersible autonomous underwater vehicle with a towfish towed by a cable. International Journal of Naval Architecture and Ocean Engineering. 2015;7(2):409–425.

[3] Lugrís U, Escalona J, Dopico D, Cuadrado J. Efficient and accurate simulation of the cable-pulley interaction in weight-lifting machines. In: Proceedings of the 1st Joint International Conference on Multibody System Dynamics, Lappeenranta, Finland; 2010. p. 1–10.

[4] Takehara S, Kawarada M, Hase K. Dynamic contact between a wire rope and a pulley using Absolute Nodal Coordinate Formulation. Machines. 2016;4(1):4.

[5] Bulín R, Hajžman M, Polach P. Nonlinear dynamics of a cable-pulley system using the absolute nodal coordinate formulation. Mechanics Research Communications. 2017;82:21–28.

[6] Čepon G, Manin L, Boltežar M. Introduction of damping into the flexible multibody belt-drive model: A numerical and experimental investigation. Journal of Sound and Vibration. 2009;324(1-2):283–296.

[7] Čepon G, Manin L, Boltežar M. Validation of a flexible multibody belt-drive model. Strojniski Vestnik Journal of Mechanical Engineering. 2011;57:539–546.

[8] Seo J, Kim S, Jung I, Park T, Mok J, Kim Y, et al. Dynamic analysis of a pantograph–catenary system using absolute nodal coordinates. Vehicle System Dynamics. 2006;44(8):615–630.

[9] Imanishi E, Nanjo T, Kobayashi T. Dynamic simulation of wire rope with contact. Journal of mechanical science and technology. 2009;23(4):1083–1088.

[10] Shabana AA. Flexible multibody dynamics: review of past and recent developments. Multibody System Dynamics. 1997;1(2):189–222.

[11] Khude NN. Efficient simulation of flexible body systems with frictional contact/impact [Ph.D. thesis]. University of Wisconsin-Madison; 2015.

[12] Berzeri M, Shabana AA. Development of simple models for the elastic forces in the absolute nodal co-ordinate formulation. Journal of Sound and Vibration. 2000;235(4):539–565.

[13] Yue Z, Yang Z, Tan C, Liu Y. The strain coupling problem and model decoupling of ANCF cable/beam element. Chinese Journal of Theoretical and Applied Mechanics. 2016;48(6):1406.

[14] Aamo O, Fossen T. Finite element modelling of moored vessels. Mathematical and Computer Modelling of Dynamical Systems. 2001;7(1):47–75.

[15] Liu M, Gorman DG. Formulation of Rayleigh damping and its extensions. Computers & Structures. 1995;57(2):277–285.

[16] Driscoll R, Nahon M. Mathematical modeling and simulation of a moored buoy system. In: OCEANS'96. MTS/IEEE Conference Proceedings. Prospects for the 21st Century.. vol. 1. IEEE; 1996. p. 517–523.

[17] Buckham B, Nahon M, Seto M, Zhao X, Lambert C. Dynamics and control of a towed underwater vehicle system, part I: model development. Ocean Engineering. 2003;30(4):453–470.

[18] Yoerger D, Grosenbaugh M, Triantafyllou M, Burgess J. Drag forces and flow-induced vibrations of a long vertical tow cable – Part I: Steady-state towing conditions. Journal of Offshore Mechanics and Arctic Engineering. 1991;113(2):117–127.

[19] Vandiver JK. Drag coefficients of long flexible cylinders. In: Offshore Technology Conference. Offshore Technology Conference; 1983. p. 1–10.

[20] Sumer BM, Fredsøe J. Hydrodynamics around Cylindrical Strucures. Singapore: World Scientific; 2006.

[21] Hunt KH, Crossley FRE. Coefficient of restitution interpreted as damping in vibroimpact. Journal of Applied Mechanics. 1975;42(2):440–445.

[22] Machado M, Moreira P, Flores P, Lankarani HM. Compliant contact force models in multibody dynamics: Evolution of the Hertz contact theory. Mechanism and Machine Theory. 2012;53:99–121.

[23] Westin C, Irani RA. Vortex-Induced Vibrations of a Low-tension Cable-Sheave System Modeled using Nonlinear Finite Elements. In: Proceedings of the 2018 CSME International Congress. Canadian Society of Mechanical Engineers; 2018. p. 1–6.

[24] Shabana AA. Dynamics of multibody systems. 3rd ed. Cambridge, UK: Cambridge University Press; 2010.

[25] Baumgarte J. Stabilization of constraints and integrals of motion in dynamical systems. Computer methods in applied mechanics and engineering. 1972;1(1):1–16.

[26] Braun DJ, Goldfarb M. Eliminating constraint drift in the numerical simulation of constrained dynamical systems. Computer Methods in Applied Mechanics and Engineering. 2009;198(37-40):3151–3160.

[27] Calnan C, Bauer RJ, Irani RA. Controller design and motion compensation for marine towed bodies. In: OCEANS 2016 MTS/IEEE Monterey. IEEE; 2016. p. 1–9.

[28] Calnan C, Bauer RJ, Irani RA. Reference-point algorithms for active motion compensation of towed bodies. IEEE Journal of Oceanic Engineering. 2018;44(4):1024–1040.

[29] Cummins W. The impulse response function and ship motions. David Taylor Model Basin Washington DC; 1962.

[30] McTaggart K. ShipMo3D version 3.0 user manual for computing ship motions in the time and frequency domains. Defence Research and Development Canada; 2011. TM 2011-308.

[31] Westin C, Irani RA. Cable-Pulley Interaction with Dynamic Wrap Angle Using the Absolute Nodal Coordinate Formulation. In: Proceedings of the 4th International Conference on Control, Dynamic Systems, and Robotics, Toronto, Canada; 2017. p. 1–10.

[32] Westin C. Modelling and Simulation of Marine Cables with Dynamic Winch and Sheave Contact [Master's thesis]. Carleton University; 2018.

[33] Takehara S, Terumichi Y, Sogabe K. Motion of a submerged tether subject to large deformations and displacements. Journal of System Design and Dynamics. 2011;5(2):296–305.

[34] Arney AM. FFG-7 Ship Motion and Airwake Trial. Part II. Removal of Ship Motion Effects from Measured Airwake Data. Melbourne, Australia: Defence Science and Technology Organization; 1994.

[35] Calnan C. Set-point algorithms for active heave compensation of towed bodies [Master's thesis]. Dalhousie University; 2016.

[36] Blevins RD. Formulas for Dynamics, Acoustics and Vibration. John Wiley & Sons; 2015.

[37] MatWeb. Overview of materials for Nylon 66, Unreinforced; 2018. [Online] Available: http://www.matweb.com/search/datasheet.aspx?matguid=a2e79a3451984d58a8a442c37a226107.

[38] McTaggart K. Validation of ShipMo3D Version 3.0 User Applications for Simulation of Ship Motions; 2012.

[39] Wall A, McTaggart K, Thornhill E, Comeau P, Lee R, McTavish S. Opportunities for expanding shipboard-helicopter operational envelopes using modelling and simulation tools;.

[40] U.S. Navy Wire-Rope Handbook Volume 1. Naval Sea Systems Command; 1976. ADA955305.

[41] Latchman S. Effect of Cable and Towbody Parameters on Tension and Cable Length when Towing at 200 m depths and 10 knots. In: Proceedings of OCEANS'93. IEEE; 1993. p. 491–496.

[42] Hoerner SF. Fluid-Dynamic Drag: Theoretical, Experimental and Statistical information. Hoerner Fluid Dynamics; 1965.

[43] Anderson Jr JD. Fundamentals of Aerodynamics. Tata McGraw-Hill Education; 2010.

[44] Sarpkaya T. Periodic Flow about Bluff Bodies Part. 1. Forces on Cylinders and Spheres in a Sinusoidally Oscillating Fluid, Naval Postgraduate School, Calif, Rep No NPS-59, SL. 1974;74091.

[45] Ramberg SE, Griffin OM. Free vibrations of taut and slack marine cables. Journal of the Structural Division. 1977;103(11).

[46] Barbieri N, de Souza Jr OH, Barbieri R. Dynamical analysis of transmission line cables. Part 1 – linear theory. Mechanical Systems and Signal Processing. 2004;18(3):659–669.

[47] Zhu Z, Meguid S. Nonlinear FE-based investigation of flexural damping of slacking wire cables. International Journal of Solids and Structures. 2007;44(16):5122–5132.